Diffractive Imaging of Conical Intersections Amplified by Resonant Infrared Fields

Diffractive Imaging of Conical Intersections Amplified by Resonant Infrared Fields

Keefer D.;Rouxel J. R.;Aleotti F.;Segatta F.;Garavelli M.;Mukamel S.

***J. Am. Chem. Soc.* 2021, 143, 34, 13806–13815**

The final published version is available online at: *https://dx.doi.org/10.1021/jacs.1c06068*

Diffractive Imaging of Conical Intersections Amplified by Resonant Infrared Fields

Daniel Keefer,[†] Jérémy R. Rouxel,[‡] Flavia Aleotti,[¶] Francesco Segatta,[¶] Marco Garavelli,[¶] and Shaul Mukamel[*,†]

[†]*Departments of Chemistry and Physics & Astronomy, University of California, Irvine, California 92697-2025, USA*

[‡]*University Lyon, UJM-Saint-Étienne, CNRS, Graduate School Optics Institute, Laboratoire Hubert Curien UMR 5516, Saint-Étienne 42023, France*

[¶]*Dipartimento di Chimica Industriale, Università degli Studi di Bologna, Viale del Risorgimento 4, I-40136 Bologna, Italy*

E-mail: smukamel@uci.edu

Abstract

The fate of virtually all photochemichal reactions is determined by conical intersections. These are energetically degenerate regions of molecular potential energy surfaces that strongly couple electronic states thereby enabling fast relaxation channels. Their direct spectroscopic detection relies on weak features that are often buried beneath stronger, less interesting contributions. For azobenzene photoisomerization, a textbook photochemical reaction, we demonstrate how a resonant infrared field can be employed during the conical intersection passage to significantly enhance its coherence signatures, while leaving the product yield intact. This transition–state amplification holds promise to bring imaging of conical intersections through time–resolved X–ray diffraction above the detection threshold.

Introduction

Recent advances in X–ray light sources, especially at free–electron lasers (FELs), offer novel windows into molecular dynamics.[1] A particularly powerful technique is time–resolved X–ray diffraction (XRD).[2–4] Traditionally used for structure determination in stationary molecular samples, the peak brilliance of X–rays has consistently been increased to allow for smaller and smaller crystal sizes.[5,6] Once the goal of pushing XRD to the single molecule limit is achieved,[5,7] direct imaging of ultrafast photochemistry will be possible.[8,9]

X–ray photons scatter off the electronic charge density. Since molecules undergoing a photochemical transformation are in a non–stationary superposition of electronic and vibrational states, there are many overlapping contributions to the diffraction pattern.[3] Disentangling them is necessary to unravel the mechanism of a photochemical process. This could mean maximizing the scattering from the excited state electron density, allowing the structure determination of individual electronic states.

The direct imaging of conical intersections (CoIns)[10,11] is an even more intriguing possibility. These are regions in the molecular landscape where electronic states are very close in energy and thus strongly coupled to nuclear motions that occur on a similar timescale. A series of pioneering ultrafast pump–probe spectroscopic experiments in the past has induced a paradigm shift in our understanding of photochemical reactions.[12–14] A sudden change in absorption features is observed on the femtosec-

ond (1 fs = 10^{-15} s) timescale once the molecule relaxes from one electronic state to another. CoIns are now widely recognized as the decisive events in ultrafast molecular transformations such as the primary event of vision.[13] They occur in every polyatomic molecule and promote radiationless transitions between excited states. The energy, topology, abundance and accessibility of conical intersections, and what quantum pathways they connect, thus determine the fate of photochemical processes. Once a nuclear wavepacket, initially located in one electronic state, reaches the CoIn, it branches and partly relaxes to other electronic states. A vibronic coherence characterized by the overlap of the nuclear wavepackets at two surfaces then emerges and persists for a short amount of time. This unique spectroscopic signature of the CoIn is generally much weaker than that of the state populations and is hard to detect.

In the XRD signal, coherences contribute by combined elastic/inelastic photon scattering from the electronic transition density.[3,4] Once isolated, this term could provide a spatial image of the conical intersection and thereby direct insight into the determining events of molecular photochemistry. A major difficulty is that the coherence magnitude is much weaker compared to elastic scattering from electronic states and thus it is buried in the total signal.

In this simulation study, we show how to significantly enhance the coherence signal and thereby offer a potential solution to this problem. The time–resolved diffraction patterns for the textbook *cis* → *trans* photoisomerization of azobenzene involving a CoIn passage are simulated. An infrared (IR) laser field resonant with the electronic transition in the CoIn region is employed. By slightly shifting around populations between the excited states, the coherence is significantly enhanced, while leaving the natural photochemistry virtually intact.

Previous studies that employed coherent infrared (IR) light fields at CoIns have aimed at controlling the photochemistry by playing with the carrier-envelope phase of the pulse[15,16] or by altering the CoIn topology through the dynamic Stark effect and thus influencing the photochemical outcome.[17] Here, rather than controlling the photochemistry, we focus on in its non–invasive imaging. Our approach demonstrates a novel utilization of IR laser pulses at conical intersections that can enable their imaging. This transition-state imaging is analogous to Zewail's transition state spectroscopy.[18] Optimal control theory (OCT)[19,20] is employed to optimize laser pulses for coherence maximization. To record a holistic imaging of molecular photochemistry, OCT is also employed to maximize other contributions in the ultrafast XRD signal, allowing for e.g. selective structure determination of excited states.

Diffraction Signal of Azobenzene Photoisomerization

Being switchable between both isomers with a high quantum yield,[21–23] azobenzene has found numerous applications in fields like material science, photopharmacology[24] or optogenetics.[25] Besides its practical relevance, the photochemical mechanism applies to many other molecules, giving our proposed scheme a broad relevance.

An effective Hamiltonian with two nuclear degrees of freedom for nuclear wavepacket simulations of azobenzene *cis* → *trans* isomerization has been introduced recently.[4,26] The first coordinate is the CNNC torsion angle between the two central nitrogen and the connected carbon atoms, connecting the *cis* geometry at CNNC = 0° and the *trans* at CNNC = 180°. The second coordinate is the CNN bending angle between the two nitrogen atoms and one adjacent carbon atom, while the other CNN angle remains fixed. Initially, both CNN angles are at 116° for the *cis* structure, and symmetry breaking is necessary to reach the minimum energy CoIn around CNNC = 94°. High–level CASPT2 excited state quantum chemical calculations in this two–dimensional space were performed to obtain the potential energy surfaces (PESs) depicted in Fig. 1.[4,26]

Two-mode models with two or more states have a long history of success in the simulation of ultrafast non-adiabatic dynamics and interpretation of corresponding experiments. Two widely recognized examples are the pyrazine

photorelaxation model of Domcke and coworkers[27] and the rhodopsin model of Hahn and Stock.[28] The latter is especially closely related to azobenzene, as it describes a photoisomerization involving a torsion and a bending angle. Its validity is corroborated by repeated applications to date.[29] Even from experimental data two-mode models were concluded to adequately describe reactive torsional dynamics, like in the case of molecular motors.[30] More general two-mode models are commonly used to simulate and describe fundamental effects of CoIn dynamics,[31,32] since a minimum of two modes is required to form a CoIn. The concept of reactive coordinates in general has been put forward for the photochemical ring opening (another textbook photochemical process) reproducing experimental data.[33] This is in general justified for ultrafast reactions since within these timescales, upon photoexcitation, the molecular motion is coherently funneled into the reactive pathways. At later times (typically after a few hundred fs), internal vibrational relaxation to other modes takes place, not being captured by such Hamiltonians. Many more nuclear modes (up to few tens) can be treated by the multi-configurational time-dependent Hartree (MCTDH) method,[34] being a more approximate approach to nuclear quantum dynamics and showing broad success.

In our effective Hamiltonian for azobenzene photoisomerization, two electronic states, the ground state S_0 and the first excited state S_1 that has $n\pi^*$ character, contribute to the process. The PESs are depicted in Fig. 1B, with the CoIn region marked in black and the nuclear wavepacket drawn in red. Initially, the wavepacket is located in the *cis* minimum of S_0. Upon electronic excitation, the wavepacket mostly is located in S_1, thanks to a non–vanishing transition dipole moment between the two states. It first evolves to larger CNN angles and then moves predominantly along the reactive CNNC torsion. This is possible due to favorable energy gradients in S_1 while in S_0 the isomerization pathway is blocked by a large 1.5 eV barrier. At 105 fs after excitation, the nuclear wavepacket reaches the S_1/S_0 CoIn. This is the decisive event common to

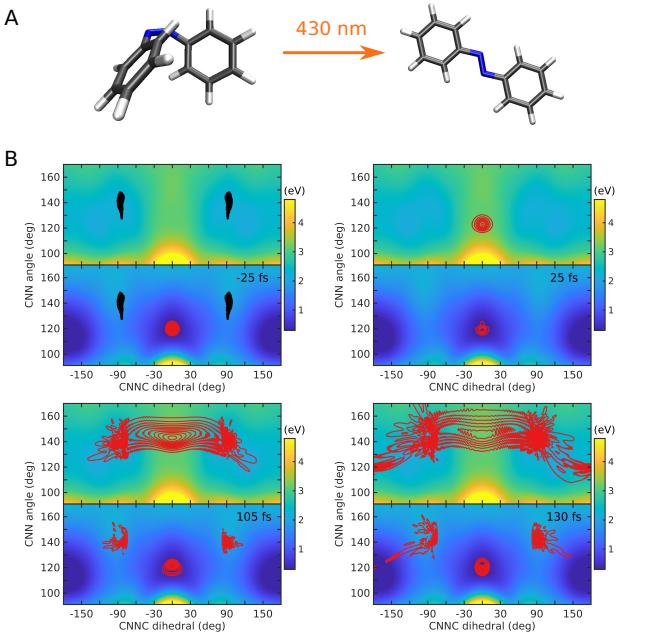

Figure 1: **A** *cis* → *trans* isomerization of azobenzene initiated by a 430 nm light field. **B** The four panels depict the potential energy surfaces of the S_0 (bottom) and S_1 state (top) along the nuclear degrees of freedom. In the top left panel, the conical intersection seam connecting both electronic states is sketched in black as the regions where the non–adiabatic coupling is non–vanishing. The nuclear wavepacket (red) starts at the *cis* minimum in S_0. Applying the laser pump shown in Fig. 3A initiates the isomerization dynamics as shown in the other three panels at 25, 105 and 130 fs.

many other photochemical reactions. Initially located only in S_1 around the CoIn, parts of the wavepacket relax into S_0 and then continue to evolve towards the *trans* geometry at $\pm 180°$, where the photochemical reaction is completed. A vibronic coherence, characterized by an overlap of nuclear wavepackets in the two electronic states, emerges around the CoIn. The initial absence and subsequent emergence of this coherence is a unique signature of CoIns and is our target for spectroscopic detection.

The ultrafast XRD imaging of molecular dynamics is sketched in Fig. 2A. First, an optical pump excites the molecule from S_0 to S_1 thus initiating the photochemistry. After a variable time–delay T, an X–ray pulse with wave vector $\boldsymbol{k}_x$ that is off–resonant with respect to all molecular transitions is scattered off the electron density. The scattered photons $\boldsymbol{k}_s$ are recorded on the detector versus the momentum transfer $\boldsymbol{q} = \boldsymbol{k}_s - \boldsymbol{k}_x$, yielding a diffraction pattern. In the absence of long–range crystalline order, the usually dominating Bragg–peaks vanish and the pattern is more smooth.

The loop diagrams in Fig. 2B represent all terms that contribute to the diffraction signal in a two–electronic–states model system. They can be partitioned into three classes. The first is elastic and inelastic scattering from the ground state, and the second from the excited state. Both classes are based on the populations $\rho_{ii}\langle\chi_i|\chi_i\rangle$ with $i = \{e, g\}$ of the normalized nuclear wavepackets $|\chi_i\rangle$ in the respective state i. The third class involves the coherences $\rho_{eg}\langle\chi_e|\chi_g\rangle$, characterized by a nuclear wavepacket overlap that is intrinsically much weaker. Additionally, the population terms include scattering from electronic state densities $\hat{\sigma}_{ii}(q)$, where all 96 electrons of the azobenzene molecule contribute. In contrast, the purely–electronic coherence terms also contain inelastic scattering from transition densities $\hat{\sigma}_{ij}(q)$ where only one (or a few) active electrons that corresponds to the excitation character (here, an electron from a nitrogen n–orbital) contribute.

The diffraction signal represented by diagrams (i)–(v) in Fig. 2B is given by

$$
\begin{aligned}
S_1(\boldsymbol{q}, T) \propto N \int dt |E_x(t-T)|^2 & \\
\rho_{gg}(t)\langle\chi_g(t)|\hat{\sigma}^\dagger_{gg}\hat{\sigma}_{gg}|\chi_g(t)\rangle & \quad \text{(i)} \\
+\rho_{ee}(t)\langle\chi_e(t)|\hat{\sigma}^\dagger_{ee}\hat{\sigma}_{ee}|\chi_e(t)\rangle & \quad \text{(ii)} \\
+\rho_{gg}(t)\langle\chi_g(t)|\hat{\sigma}^\dagger_{ge}\hat{\sigma}_{eg}|\chi_g(t)\rangle & \quad \text{(iii)} \\
+\rho_{ee}(t)\langle\chi_e(t)|\hat{\sigma}^\dagger_{eg}\hat{\sigma}_{ge}|\chi_e(t)\rangle & \quad \text{(iv)} \\
+2\mathcal{R}\left[\rho_{eg}(t)\langle\chi_e(t)|\hat{\sigma}^\dagger_{ee}\hat{\sigma}_{eg}|\chi_g(t)\rangle\right. & \quad \text{(v)} \\
\left.+\,\rho_{eg}(t)\langle\chi_e(t)|\hat{\sigma}^\dagger_{eg}\hat{\sigma}_{gg}|\chi_g(t)\rangle\right]. & \quad (1)
\end{aligned}
$$

It depends on the X–ray probe pulse envelope $E_x(t-T)$, taken to be a Gaussian with 2 fs full width at half maximum (FWHM), the time delay T, the number of molecules N, and we write $\hat{\sigma} = \hat{\sigma}(\boldsymbol{q}, R)$ for brevity. As indicated in Fig. 2A, we propose employing an additional IR field at the same time delay as E_x. The IR pulse amplifies the signals differentially by introducing a resonance (pole in the complex plane) at the small energy gap in the vicinity of the CoIn. Small amounts of population in this region are shifted around between the two electronic states, enhancing the wavepacket overlap and thus the coherence. In our simulations, the IR field is included in the propagation of $\chi(t)$ and thus does not appear explicitly in the signal expression (Eq. 1). In Eq. 2 and the SI we derive perturbative expressions in the IR field by including it at the signal stage but not in the propagation, leading to an amplification term when it is resonant with the energy gap around the CoIn.

The σ_{ij} in Eq. 1 remain operators in the nuclear space after taking their matrix elements in the adiabatic electronic subspace. Once recorded in momentum space, stationary diffraction patterns can be translated to real–space to obtain the electron density $\hat{\sigma}(\boldsymbol{r})$ and thereby the molecular structure. There are a few problems with this inversion, i.e. the phase problem related to the fact that only absolute amplitudes are recorded and the phases are therefore lost. An extensive literature exists that solves this problem e.g. by oversampling,[35] or by anomalous diffraction.[36] Phase retrieval for structure reconstruction is still scarce in

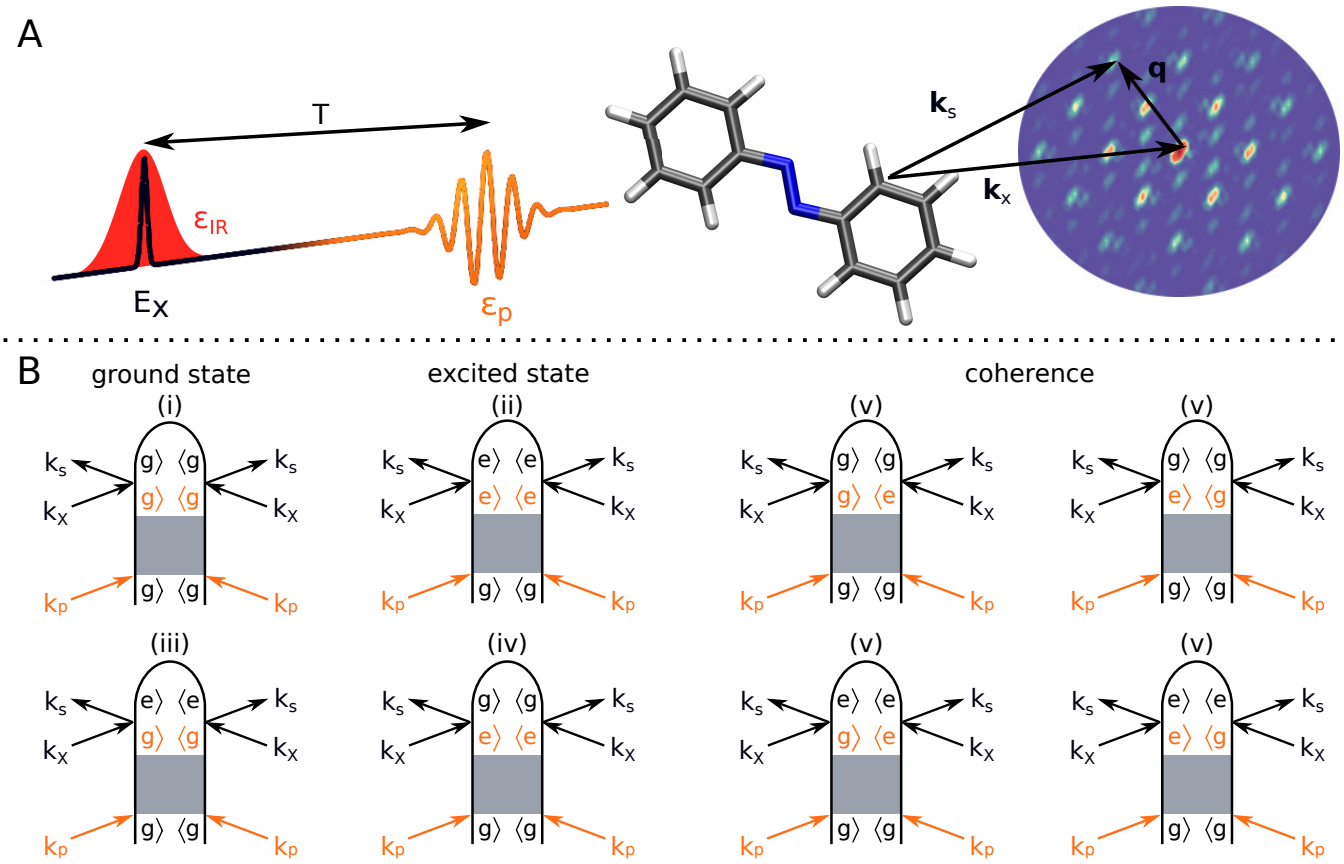

Figure 2: **A** Ultrafast X–ray diffraction. A pump pulse ε_p excites azobenzene and initiates the photoisomerization in S_1. A time–delayed X–ray probe pulse with envelope E_x images the molecular structure by elastic and inelastic photon scattering. An additional resonant infrared field significantly enhances the coherence, while leaving the product yield unaffected. **B**: Loop diagrams of the single–molecule diffraction signal. Diagram rules are given in the SI. Labeling of the individual loops (i)–(v) corresponds to Eq. 1

femtosecond X-ray diffraction studies as this is a difficult task with many technical subtleties and pitfalls. Nonetheless, phase reconstruction is being achieved in increasingly more challenging situations.[37–40] It is not clear which method is most suitable for phase retrieval in our proposed experiment. Here, we focus on predicting and explaining what can be learned about CoIns from the diffraction patterns. Recently, we have shown that oscillations in the coherence term (v) in Eq. 1 correspond to phase changes of the electron transition density in real–space.[4]

While Eq. 1 yields the total diffraction pattern that monitors the photochemical reaction, it is desirable to isolate contributions of individual diagrams. Structure determination in the ground state is straightforward, and separate imaging of excited state structures could be enabled by targeting terms (ii) and (iv). The most intriguing possibility is the direct imaging of the charge density at CoIns by isolating term (v).

We employ OCT[19,20] to investigate both excited state and coherence amplification possibilities. In this approach, laser pulses are usually shaped to prepare a targeted quantum state at a desired time. Numerous other control aims have been achieved experimentally in chemistry[41,42] and biology,[43,44] demonstrating the potential of laser-steered molecular dynamics. Technically, the algorithm works via iterative maximization of a global control functional[45,46] by shaping the temporal structure of the controlling laser field. OCT holds promise to directly amplify spectroscopic features as well,[47,48] as will be demonstrated here. By examining the loop diagrams of the XRD signal in Fig. 2B, we identify three groups of diagrams that can potentially be maximized at desired times. The first is diagrams (i) and (iii) related to the ground state population $|g\rangle\langle g|$ and is trivially achieved by removing the optical pump ε_p, leaving azobenzene in the electronic ground state. The second group consists of diagrams (ii) and (iv), associated with the excited state population $|e\rangle\langle e|$. This means shaping ε_p to achieve maximum population transfer from S_0 to S_1, potentially enabling direct excited state structure determination. The third group (diagrams (v)) is the most interesting for us and involves the coherences $|g\rangle\langle e|$. Being buried in the total diffraction signal by elastic scattering from $|g\rangle\langle g|$ and $|e\rangle\langle e|$, maximization of this contribution should enable the direct imaging of conical intersection charge densities.

Theoretical Selection of Quantum Pathways

We first explore the optimization of individual quantum pathways that contribute to the XRD signal. OCT[20] is employed to tailor laser pulses that prepare specific states associated with these pathways at specified times. Our first optimization aim is to prepare the $|e\rangle\langle e|$ state, such that pathways (ii) and (iv) and thereby scattering from the electronically excited state dominates the total XRD signal. This is accomplished by employing an optical laser field with a wavelength tuned to the S_0 to S_1 transition, which is around 430 nm for the *cis* geometry of azobenzene. Starting with a Gaussian laser field envelope, the optimized laser pulse that maximizes $|e\rangle\langle e|$ at 25 fs, i.e. shortly after the pulse in time, is shown if Fig. 3A. It has an almost perfect Gaussian envelope with a FWHM of 10 fs and achieves 80% population transfer from S_0 to S_1. Higher yields are possible but come at the cost of increased pulse intensity and complexity, which might initiate undesired multi–photon processes. In a recent diffraction experiment on the retinal photoisomerization in bacteriorhodopsin,[49] a power titration of the optical pump had found that deviation from the linear regime occurs at about 30 GW cm^{-2}. Our pump pulse in Fig. 3A exhibits an electric field strength of around 6 GV/cm, which amounts to an intensity of below 5 GW cm^{-2}. Multi–photon processes are thus unlikely, and 80% excitation is sufficient to achieve a dominating $|e\rangle\langle e|$ contribution in the diffraction signal. This is demonstrated in Fig. 4, which depicts the total diffraction signal using the pulse of Fig. 3A, together with the relative magnitude of the elastic excited state scattering term (ii) in Eq. 1. Initially vanishing prior to the pump, this relative magnitude gets

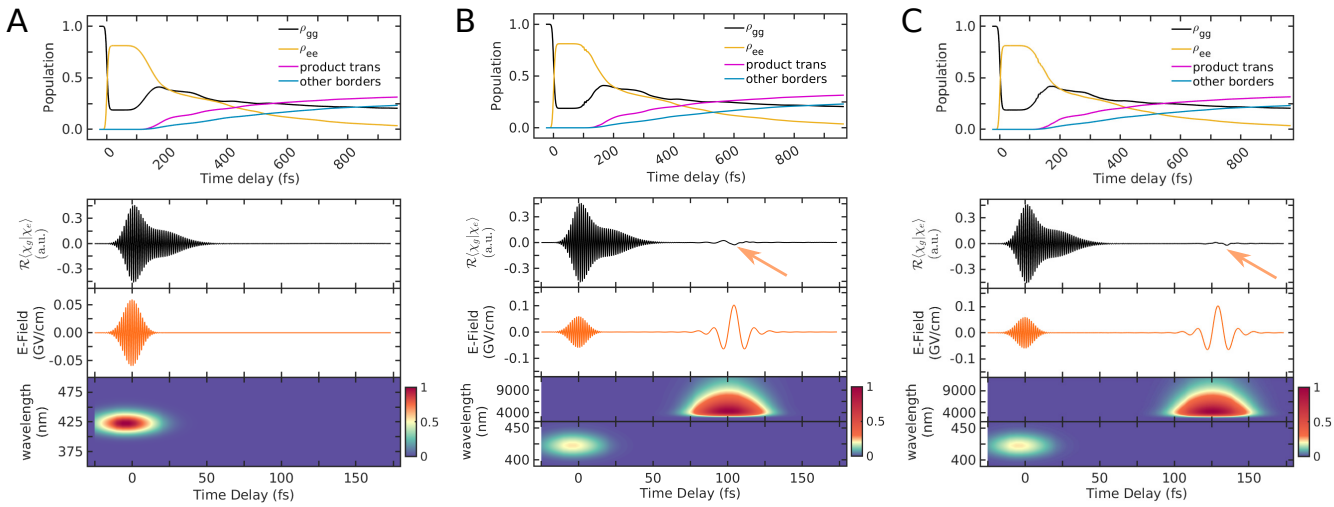

Figure 3: **A** Population dynamics (top), coherence magnitudes (black), laser pulses (orange) and spectrograms (bottom) using only a visible field. **B**: with additional IR field at 105 fs delay. **C**: with IR field at 130 fs delay. The additional IR field in B and C enhances the coherence magnitude, while leaving the population dynamics and thus the photochemical reaction intact.

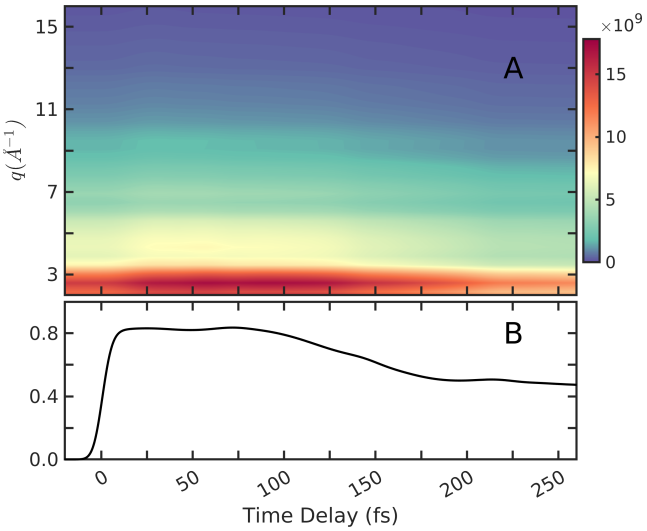

Figure 4: **A**: Total radially averaged diffraction signal (Eq. 1) during the isomerization dynamics. **B**: Relative magnitude of the excited state contribution (term (ii) in Eq. 1) integrated over $\boldsymbol{q}$ as it is almost constant along $\boldsymbol{q}$. Achieving efficient population transfer by quantum control allows for structure determination from the excited state.

very large, and dominates the diffraction signal after the action of ε_p. The total diffraction signal does not change yet, since the ground and excited state electron densities are very similar, and the nuclear wavepacket is located at the same geometry. Nevertheless, between 0 and 150 fs, it is mainly dominated by term (ii) in Eq. 1, allowing for the transient monitoring of excited state structures on the photochemical pathway.

Note that practically, in typical "*laser on* minus *laser off*" experiments, the ground state contribution could simply be subtracted to obtain the excited state signal without any shaping. As demonstrated in recent similar experiments,[9,50] the detection limit for weak features still critically relies on the fraction of excited molecules. Using OCT to significantly enhance this can be beneficial. Additionally, in azobenzene *cis* $\rightarrow$ *trans* photoisomerization, only one excited state S_1 contributes to the photochemistry, and subtracting the ground state yields the contribution of this state. Other molecules and processes might involve two or more excited states, where this specificity no longer holds. Using the same OCT presented here, the population in individual states can be maximized, thus allowing for detection of their specific signatures. Referring to Fig. 2B, introducing more excited states e' adds a new group

of loop diagrams that each contribute to the total diffraction signal. Using the same OCT, each quantum pathway can be individually addressed, allowing to acquire more detailed information about the photochemical mechanism.

Besides the optimal laser pulse and its spectrogram, Fig. 3A also depicts the *cis* → *trans* photoisomerization kinetics. After initial excitation, the CoIn seam is reached at around 100 fs, and the nuclear wavepacket relaxes back to the ground state. Once reaching the product minimum of *trans* azobenzene at ±180°, it is absorbed and not considered further. The population in the *trans* minimum is marked by the magenta line in Fig. 3A and slowly reaches over 40% within 900 fs.

Our second goal is to maximize the coherence ρ_{eg} magnitude at the CoIn passage. This should enhance pathways (v) in Fig. 2 and Eq. 1. After being very strong during the optical excitation, as the wavepacket is equally distributed between S_0 and S_1 during the population transfer, ρ_{eg} is almost vanishing during the CoIn passage. As demonstrated in previous studies,[4] the coherence term is strongest at high momentum transfer amplitudes q. This is because the electron transition densities $\sigma_{ij}(\boldsymbol{r})$ are more confined in real space than the state densities $\sigma_{ii}(\boldsymbol{r})$, as only a single electron from a nitrogen orbital contributes. The quantity determining the strength of the coherence term (v) at high q is $|g\rangle\langle e|$, which we directly optimize with OCT. We use the projection operator depicted in Fig. S2 to maximize $|g\rangle\langle e|$ at 105 fs, where the major CoIn passage takes place. This projection operator restricts the evaluation of the control functional to a specific region in the nuclear space thus ensuring selectivity to the CoIn.

We first tried to optimize the optical pump ε_p by employing temporal and frequency constraints, which did not yield significant results. Instead, after removing the constraints, the algorithm converges to an additional field directly centered around 105 fs with an almost Gaussian envelope and a frequency range in the IR regime. The approach clearly works, as demonstrated in Fig. 3B. The almost vanishing coherence ρ_{eg} at 105 fs without the IR field is now greatly enhanced. Importantly, as can be seen from the population dynamics in Fig. 3B, and especially the product yield, the photochemical reaction remains intact. This ensures that the photochemical process is observed in its natural form, without modifying it during the observation. The IR field in Fig. 3B is surprisingly smooth, in contrast to the more complicated temporal profiles usually obtained after many OCT cycles. The proposed scheme is thus readily feasible and does not require an elaborate pulse shaping.

The effect of IR amplification on the diffraction signal is shown in Fig. 5. The signal (Eq. 1) is given by the radial average over molecular orientations and drawn vs time and the scattering vector $\boldsymbol{q}$. Using only the visible pump laser pulse and no IR field, the coherence term in the diffraction signal is very weak in Fig. 5A. Employing the IR field at 105 and 130 fs significantly amplifies this contribution, achieving the control aim. This is further exemplified in Fig. 5D E and F, which show the relative magnitude of the coherence term in the total diffraction signal. Being well below 10^{-3} in the absence of the IR field, and thus much weaker than other contributions and probably not detectable, this significantly changes when the IR field is employed. The coherence term is amplified by at least one order of magnitude, reaching 1% relative strength at high $\boldsymbol{q}$ and precisely at the time of the CoIn passage. In combination with other techniques for further separating the coherence term, e.g. frequency–resolved diffraction,[51] the IR field could bring this signature above the detection threshold. In recent scattering experiments, a detection limit of 0.05% for a perfectly excited sample has been reported,[50] and oscillatory features with 4% relative strength have been resolved for a weakly excited sample.[9] These numbers are comparable to the coherence term strength in Fig. 5B assuming 80% excitation, which should thus be detectable.

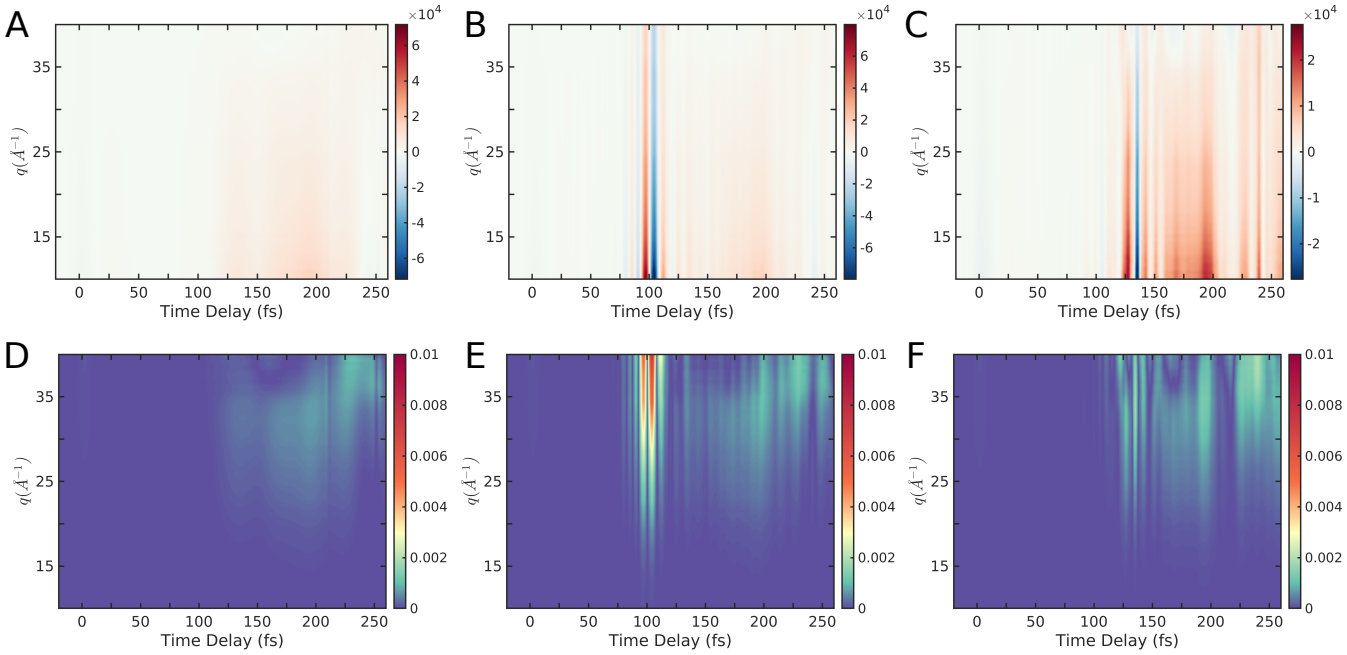

Figure 5: **A**: Coherence contribution (v) to the diffraction signal in the absence of an IR field corresponding to Fig. 3A. **B** and **C**: An additional IR field (Fig. 3B and C) is placed at 105 and 130 fs. The coherence term is clearly amplified. **D**–**F**: Relative magnitude of the coherence term (v) to the total diffraction signal corresponding to panels A, B and C.

Experimental Realizations

In experiment, only the total diffraction signal – and not the individual quantum pathways – is observed. Additionally, optimal control experiments (OCE) work fundamentally differently from OCT. While in OCT individual quantum pathways, represented by the loop diagrams in Fig. 2B, can be optimized, in OCE the control problem is solved by feeding the spectral output after sample interaction to an evolutionary algorithm, and optimizing for a desired contribution. Laser pulses are dispersed onto a liquid crystal spatial light modulator, where individual pixels can be modified to suppress specific pulse frequencies.[41,52] This major discrepancy had always complicated the practical implementation of OCT.

Here, we present a novel strategy that is directly achievable in OCE. No a priori knowledge about the CoIn is necessary. An IR field with frequencies of a few tenths of eV or below will only induce a resonant coherence amplification when the electronic states get very close in energy, i.e. exactly at CoIns. A generic IR field resembling the one in Fig. 3B can be used in coincidence with the X–ray probe field at variable time delays. Only when the molecule goes through a CoIn passage, the XRD diffraction at high momentum transfer q will exhibit oscillatory features resembling the ones in Fig. 5. This is exemplified in Figs. 3C and 5C where the pulse optimized for 105 fs is also effective at 130 fs and exhibiting a very smooth Gaussian shape. The oscillatory spectral output from Fig. 5 can then be relayed to the genetic algorithm used experimentally to optimize the IR field exactly for this feature and enhance it even more.

Once the optimal solution to this control problem is found, information about the CoIn itself can be retrieved from the pulse spectrogram. In our case, the IR field in Fig. 3 is centered around 5 μm, i.e. 0.25 eV. This exactly matches the energy difference between S_1 and S_0 at the CoIn in Fig. 1B. In this respect, the IR field does not only act as an amplification of the X–ray probe, but also as a direct probe of energetic topologies around CoIns. This approach is universally applicable to a wide range of photochemical reactions to amplify coherences and thereby decipher CoIn dynamics.

Our proposed IR control scheme works particularly well for short timescales in efficient photochemical reactions like azobenzene isomerization, where the nuclear motion is coherently funneled into specific pathways. At longer times, internal vibrational relaxation to other nuclear degrees of freedom takes place, and the molecule explores a much larger conformational space. Any near-degeneracy region between two electronic states with a non-vanishing transition dipole will then contribute to the IR-induced signal. The latter is then no longer specific to CoIns, since besides near-degeneracy, it does not depend on unique CoIn signatures like, e.g., the geometric phase,[53] for which sensitive experimental signatures have not been identified yet.

The resonant amplification via an IR field can be rationalized by including it in Eq. 1. In the SI, we derive expressions for the ultrafast XRD signal perturbed at second order by the IR field with envelope E_{IR} and central frequency ω_{IR}. The coherence term then reads

$$S_{\mathrm{XRD}}(\boldsymbol{q}, T, \omega_{\mathrm{IR}}) \propto \mathrm{Re}\frac{\boldsymbol{\mu}_{ge}\boldsymbol{\mu}_{eg}|E_{\mathrm{IR}}(\omega_{\mathrm{IR}})|^2}{(\omega_{ge} - \omega_{\mathrm{IR}} + i\epsilon)(\omega_{eg} - \omega_{\mathrm{IR}} + i\epsilon)} \int dt \rho_{eg}(t)|E_x(t-T)|^2 \times \langle \chi_e(t)|\sigma_{eg}^{\dagger}\sigma_{ee}|\chi_g(t)\rangle. \quad (2)$$

where μ_{ge} are transition dipole matrix elements between the g and e state, in this case taken to be an average over the nuclear space near the CoIn. In comparison to Eq. 1, we obtain a resonance factor when the IR field central frequency matches the average energy difference between the PES at delay T. Again, this loses specificity at longer timescales, since any near-degeneracy region in the high-dimensional nuclear space will induce a resonance factor. The advantage of the OCT scheme is that it can readily find the IR pulse central frequency that enhances the coherence contribution in the signal at a desired delay without a priori knowledge of the CoIn geometry. Alternatively, the OCT can be used to map the energy difference experienced by the wavepacket at that delay.

A competing technique to XRD at FELs is ultrafast electron diffraction (UED) at dedicated facilities.[54–59] Instead of photon pulses, ultrabright electron pulses are used to record diffraction patterns from molecules. In addition to scattering off electron densities, the electron pulses also scatter off the nuclear charge density. With respect to Eq. 1, all terms are contained in the UED signal as well, while interesting terms involving the nuclear charge density and mixed nuclear + electronic terms come into play.[3] It has been experimentally demonstrated that structural and electronic dynamics can be simultaneously recorded in a single UED experiment.[59] In particular, the retrieval of local molecular information at high momentum transfer amplitudes, as reported here for CoIns, has been demonstrated there as well by detecting the local n-hole of the nitrogen atom in pyridine. Given the similarity of the XRD and UED signal in the rigorous quantum-electrodynamical framework,[3] employed in Eq. 1, our proposed IR enhancement of molecular coherences is expected to apply to UED as well. Recent simulations of the UED signal for *trans* → *cis* isomerization of azobenzene have already demonstrated the sensitivity of this signal to ultrafast molecular motions.[60]

Summary

We demonstrated the ability of infrared fields to help the direct imaging of conical intersections. The corresponding signature in the time–resolved X–ray diffraction signal is significantly amplified by resonantly enhancing the coherence magnitude. This signature may not be observable otherwise, since the total signal is dominated by the much stronger elastic scattering contributions that give no information about conical intersections. Employing an IR field that maximizes the coherence can be the crucial factor in making direct imaging of conical intersections possible, potentially revolutionizing the understanding of ultrafast photochemistry. The results are demonstrated for azobenzene photoisomerization, which is widely applied in chemistry, biology and pharmacology, and provides a typical textbook conical intersection passage as found in many other molecules and

systems. The laser pulses are optimized with optimal control theory, ensuring their maximal success, and are surprisingly smooth and simple. The energetic topology of the conical intersection can be read from the optimized laser field spectrogram. The present approach is readily translatable to other molecules, provided that there exists a non–vanishing transition dipole in the conical intersection vicinity. The IR field leaves the photochemistry intact, and thus provides a non–invasive amplification of molecular coherences in the naturally occurring mechanism.

Methods

To perform exact nuclear wavepacket simulations of azobenzene photoisomerization, we select two reactive nuclear degrees of freedom.[4] The torsion angle between the nitrogen and the two connected carbon atoms connects the *cis* geometry at CNNC = 0° to the *trans* at CNNC = 180°, and is thus the active isomerization coordinate. The bending angle between the two nitrogen atoms and one adjacent carbon atom is the second coordinate while the other CNN angle remains fixed. This symmetry breaking is necessary in order to reach the minimum energy conical intersection seam.

The effective Hamiltonian describing the coupled nuclear and electronic degrees of freedom, in the space of the two nuclear coordinates $R1$ and $R2$, is given by

$$\hat{H} = \begin{pmatrix} \hat{T} + \hat{V}_g(\mathbf{R}) & -\varepsilon(t)\hat{\mu}_{eg}(\mathbf{R}) + \hat{K}_{ge} \\ -\varepsilon(t)\hat{\mu}_{eg}(\mathbf{R}) - \hat{K}_{eg} & \hat{T} + \hat{V}_e(\mathbf{R}) \end{pmatrix}. \tag{3}$$

The potential energy surfaces $\hat{V}(\mathbf{R})$ for the ground state g and excited state e (Fig. 1) were computed using high–level CASPT2 with an active space of 18 electrons in 16 orbitals (all π and π^{ast} orbitals and two nitrogen n-orbitals) with the MOLCAS8 program package[61] and the ANO-L-VDZP basis set.[62] They were discretized on a numerical grid with 600 points in CNNC and 256 in CNN.

The kinetic energy operator $\hat{T}$ in Eq. 3 in the G–Matrix formalism is given by[63,64]

$$\hat{T} \simeq -\frac{\hbar^2}{2m} \sum_{o=1}^{2} \sum_{p=1}^{2} \frac{\partial}{\partial q_o} \left[G_{op} \frac{\partial}{\partial q_p} \right] \tag{4}$$

with $o, p \in \mathbf{R}$ and the G-Matrix computed via its inverse elements

$$\left(G^{-1}\right)_{op} = \sum_{i=1}^{3N} m_i \frac{\partial x_i}{\partial q_o} \frac{\partial x_i}{\partial q_p} \quad . \tag{5}$$

$\hat{K}_{ge}$ in Eq. 3 approximates the non–adiabatic couplings and is given by[65]

$$\hat{K}_{ge} = \frac{1}{2m} \left(2 f_{ge} \frac{\partial}{\partial \mathbf{R}} + \frac{\partial}{\partial \mathbf{R}} f_{ge} \right) \tag{6}$$

and f_{ge} contains terms $\langle \Phi_g | \ \frac{\partial}{\partial \mathbf{R}} \Phi_e \rangle$ with the electronic wavefunction Φ .

The nuclear wavefunction $\chi(\mathbf{R}, t)$ is obtained by propagating the S_0 ground state vibrational wavefunction $\chi(\mathbf{R}, t_0)$ with a Chebychev scheme[66] using a time step of 0.05 fs. Periodic boundary conditions are employed along CNNC in S_1 while in S_0a Butterworth filter[67] absorbs the wavepacket at CNNC = ±180°. All terms (i)–(v) in the diffraction signal (Eq. 1) were evaluated ever 0.5 fs. This requires the state and transition densities $\sigma_{ij}(\mathbf{q}, \mathbf{R})$, which remain operators in the nuclear space and were evaluated in 2° increments from the state specific charge density matrices P_{rs}^{ij} according to

$$\begin{aligned} \sigma_{ij}(\mathbf{q}, \mathbf{R}) = & \int dr e^{-i\mathbf{q}\cdot\mathbf{r}} \\ & \sum_{rs} P_{rs}^{ij}(\mathbf{R}) \phi_r^*(\mathbf{r}, \mathbf{R}) \phi_s(\mathbf{r}, \mathbf{R}). \end{aligned} \tag{7}$$

using the basis set of atomic orbitals $\phi_r(\mathbf{r})$.

Laser pulses were optimized by OCT through iterative maximization of the functional[45,46]

$$\begin{aligned} & J[\psi_i(t), \psi_f(t), \varepsilon(t)] = F[\psi_i(t)] \\ & - \int_0^T s(t) |\varepsilon(t)|^2 dt - \int_0^T \psi_f(t) G[\psi_i(t), \varepsilon(t)] dt, \end{aligned} \tag{8}$$

with the initial and final wavefunctions $\psi_i(t)$ and $\psi_f(t)$, and with $G[\psi_i(t), \varepsilon(t)]$ representing the time–dependent Schrödinger equation.

$F[\psi_i(t)]$ denotes the optimization aim

$$F[\psi_i(t)] = \langle\psi_i(T)|\hat{P}|\psi_i(T)\rangle \tag{9}$$

where we use the projection operator $\hat{P} = |\psi_i\rangle\langle\psi_i|$. The function $s(t)$ in Eq. 8 contains the Krotov change parameter α that penalizes high pulse intensities,[68] a shape function to ensure smooth switching on and off behavior of the laser field, and filter operation in the frequency domain to keep the pulse within a defined spectral range.[69]

Pulse spectrograms depicted in Fig. 3 were calculated by

$$I_{FROG}(\omega, T) = \left| \int_{-\infty}^{\infty} dt\, \varepsilon(t) E_{\text{gate}}(t - T)\, e^{-i\omega t} \right|^2 . \tag{10}$$

corresponding to a frequency–resolved optical gating measurement.[?]

Acknowledgement We gratefully acknowledge support from the Chemical Sciences, Geosciences, and Bio-Sciences Division, Office of Basic Energy Sciences, Office of Science, US Department of Energy, through award DE-SC0019484. D.K. gratefully acknowledges support from the Alexander von Humboldt foundation through the Feodor Lynen program. We thank Markus Kowalewski for providing his QDng quantum dynamics code.

Supporting Information Available

The following files are available free of charge.

- Supporting PDF file: Loop diagram rules for Fig. 2B and detailed derivation of Eq. 2

References

(1) Young, L. et al. Roadmap of ultrafast x-ray atomic and molecular physics. *Journal of Physics B: Atomic, Molecular and Optical Physics* **2018**, *51*, 032003.

(2) Bennett, K.; Kowalewski, M.; Rouxel, J. R.; Mukamel, S. Monitoring molecular nonadiabatic dynamics with femtosecond X-ray diffraction. *Proceedings of the National Academy of Sciences* **2018**, *115*, 6538–6547.

(3) Rouxel, J. R.; Keefer, D.; Mukamel, S. Signatures of electronic and nuclear coherences in ultrafast molecular x-ray and electron diffraction. *Structural Dynamics* **2021**, *8*, 014101.

(4) Keefer, D.; Aleotti, F.; Rouxel, J. R.; Segatta, F.; Gu, B.; Nenov, A.; Garavelli, M.; Mukamel, S. Imaging conical intersection dynamics during azobenzene photoisomerization by ultrafast X-ray diffraction. *Proceedings of the National Academy of Sciences of the United States of America* **2021**, *118*, e2022037118.

(5) Chapman, H. N. et al. Femtosecond X-ray protein nanocrystallography. *Nature* **2011**, *470*, 73–77.

(6) Chapman, H. N. X-Ray Free-Electron Lasers for the Structure and Dynamics of Macromolecules. *Annual Review of Biochemistry* **2019**, *88*, 35–58.

(7) Neutze, R.; Wouts, R.; van der Spoel, D.; Weckert, E.; Hajdu, J. Potential for biomolecular imaging with femtosecond X-ray pulses. *Nature* **2000**, *406*, 752–757.

(8) Stankus, B.; Yong, H.; Ruddock, J.; Ma, L.; Carrascosa, A. M.; Goff, N.; Boutet, S.; Xu, X.; Zotev, N.; Kirrander, A.; Minitti, M. P.; Weber, P. M. Advances in ultrafast gas-phase x-ray scattering. *Journal of Physics B: Atomic, Molecular and Optical Physics* **2020**, *53*, 234004.

(9) Yong, H. et al. Observation of the molecular response to light upon photoexcitation. *Nature Communications* **2020**, *11*, 2157.

(10) Yarkony, D. R. Diabolical conical intersections. *Reviews of Modern Physics* **1996**, *68*, 985–1013.

(11) Domcke, W.; Yarkony, D. R.; Köppel, H. *Conical Intersections*; Advanced Series in Physical Chemistry; WORLD SCIENTIFIC, 2011; Vol. 17; pp i–xiii.

(12) Lim, J. S.; Kim, S. K. Experimental probing of conical intersection dynamics in the photodissociation of thioanisole. *Nature Chemistry* **2010**, *2*, 627–632.

(13) Polli, D.; Altoè, P.; Weingart, O.; Spillane, K. M.; Manzoni, C.; Brida, D.; Tomasello, G.; Orlandi, G.; Kukura, P.; Mathies, R. A.; Garavelli, M.; Cerullo, G. Conical intersection dynamics of the primary photoisomerization event in vision. *Nature* **2010**, *467*, 440–443.

(14) Martinez, T. J. Seaming is believing. *Nature* **2010**, *467*, 412–413.

(15) Kübel, M.; Siemering, R.; Burger, C.; Kling, N. G.; Li, H.; Alnaser, A. S.; Bergues, B.; Zherebtsov, S.; Azzeer, A. M.; Ben-Itzhak, I.; Moshammer, R.; de Vivie-Riedle, R.; Kling, M. F. Steering Proton Migration in Hydrocarbons Using Intense Few-Cycle Laser Fields. *Physical Review Letters* **2016**, *116*, 193001.

(16) Schnappinger, T.; de Vivie-Riedle, R. Coupled nuclear and electron dynamics in the vicinity of a conical intersection. *The Journal of Chemical Physics* **2021**, *154*, 134306.

(17) Sussman, B. J.; Townsend, D.; Ivanov, M. Y.; Stolow, A. Dynamic Stark Control of Photochemical Processes. *Science* **2006**, *314*, 278–281.

(18) Polanyi, J. C.; Zewail, A. H. Direct Observation of the Transition State. *Accounts of Chemical Research* **1995**, *28*, 119–132.

(19) Judson, R. S.; Rabitz, H. Teaching lasers to control molecules. *Physical Review Letters* **1992**, *68*, 1500–1503.

(20) Rabitz, H.; de Vivie-Riedle, R.; Motzkus, M.; Kompa, K.-L. Whither the Future of Controlling Quantum Phenomena? *Science* **2000**, *288*, 824–828.

(21) Nägele, T.; Hoche, R.; Zinth, W.; Wachtveitl, J. Femtosecond photoisomerization of cis-azobenzene. *Chemical Physics Letters* **1997**, *272*, 489–495.

(22) Schultz, T.; Quenneville, J.; Levine, B.; Toniolo, A.; Martínez, T. J.; Lochbrunner, S.; Schmitt, M.; Shaffer, J. P.; Zgierski, M. Z.; Stolow, A. Mechanism and Dynamics of Azobenzene Photoisomerization. *Journal of the American Chemical Society* **2003**, *125*, 8098–8099.

(23) Nenov, A.; Borrego-Varillas, R.; Oriana, A.; Ganzer, L.; Segatta, F.; Conti, I.; Segarra-Marti, J.; Omachi, J.; Dapor, M.; Taioli, S.; Manzoni, C.; Mukamel, S.; Cerullo, G.; Garavelli, M. UV-Light-Induced Vibrational Coherences: The Key to Understand Kasha Rule Violation in trans -Azobenzene. *The Journal of Physical Chemistry Letters* **2018**, *9*, 1534–1541.

(24) Broichhagen, J.; Frank, J. A.; Trauner, D. A Roadmap to Success in Photopharmacology. *Accounts of Chemical Research* **2015**, *48*, 1947–1960.

(25) DiFrancesco, M. L. et al. Neuronal firing modulation by a membrane-targeted photoswitch. *Nature Nanotechnology* **2020**, *15*, 296–306.

(26) Aleotti, F.; Soprani, L.; Nenov, A.; Berardi, R.; Arcioni, A.; Zannoni, C.; Garavelli, M. Multidimensional Potential Energy Surfaces Resolved at the RASPT2 Level for Accurate Photoinduced Isomerization Dynamics of Azobenzene. *Journal of Chemical Theory and Computation* **2019**, *15*, 6813–6823.

(27) Woywod, C.; Domcke, W.; Sobolewski, A. L.; Werner, H. Characterization of the S 1 âĂŞ S 2 conical intersection in pyrazine using ab initio multiconfiguration selfâĂŘconsistentâĂŘfield and multireference configurationâĂŘinteraction methods. *The*

Journal of Chemical Physics **1994**, *100*, 1400–1413.

(28) Hahn, S.; Stock, G. Quantum-Mechanical Modeling of the Femtosecond Isomerization in Rhodopsin. *The Journal of Physical Chemistry B* **2000**, *104*, 1146–1149.

(29) Marsili, E.; Olivucci, M.; Lauvergnat, D.; Agostini, F. Quantum and Quantum-Classical Studies of the Photoisomerization of a Retinal Chromophore Model. *Journal of Chemical Theory and Computation* **2020**, *16*, 6032–6048.

(30) Conyard, J.; Addison, K.; Heisler, I. A.; Cnossen, A.; Browne, W. R.; Feringa, B. L.; Meech, S. R. Ultrafast dynamics in the power stroke of a molecular rotary motor. *Nature Chemistry* **2012**, *4*, 547–551.

(31) Duan, H.-G.; Thorwart, M. Quantum Mechanical Wave Packet Dynamics at a Conical Intersection with Strong Vibrational Dissipation. *The Journal of Physical Chemistry Letters* **2016**, *7*, 382–386.

(32) Dey, D.; Henriksen, N. E. On Weak-Field (One-Photon) Coherent Control of Photoisomerization. *The Journal of Physical Chemistry Letters* **2020**, *11*, 8470–8476.

(33) Hofmann, A.; de Vivie-Riedle, R. Quantum dynamics of photoexcited cyclohexadiene introducing reactive coordinates. *The Journal of Chemical Physics* **2000**, *112*, 5054–5059.

(34) Worth, G. A.; Meyer, H.-D.; Köppel, H.; Cederbaum, L. S.; Burghardt, I. Using the MCTDH wavepacket propagation method to describe multimode non-adiabatic dynamics. *International Reviews in Physical Chemistry* **2008**, *27*, 569–606.

(35) Miao, J.; Charalambous, P.; Kirz, J.; Sayre, D. Extending the methodology of X-ray crystallography to allow imaging of micrometre-sized non-crystalline specimens. *Nature* **1999**, *400*, 342–344.

(36) Son, S.-K.; Chapman, H. N.; Santra, R. Multiwavelength Anomalous Diffraction at High X-Ray Intensity. *Physical Review Letters* **2011**, *107*, 218102.

(37) Chen, C.-C.; Miao, J.; Wang, C. W.; Lee, T. K. Application of optimization technique to noncrystalline x-ray diffraction microscopy: Guided hybrid input-output method. *Physical Review B* **2007**, *76*, 064113.

(38) Gaffney, K. J.; Chapman, H. N. Imaging Atomic Structure and Dynamics with Ultrafast X-ray Scattering. *Science* **2007**, *316*, 1444–1448.

(39) Abbamonte, P.; Wong, G. C. L.; Cahill, D. G.; Reed, J. P.; Coridan, R. H.; Schmidt, N. W.; Lai, G. H.; Joe, Y. I.; Casa, D. Ultrafast Imaging and the Phase Problem for Inelastic X-Ray Scattering. *Advanced Materials* **2010**, *22*, 1141–1147.

(40) Clark, J. N.; Beitra, L.; Xiong, G.; Higginbotham, A.; Fritz, D. M.; Lemke, H. T.; Zhu, D.; Chollet, M.; Williams, G. J.; Messerschmidt, M.; Abbey, B.; Harder, R. J.; Korsunsky, A. M.; Wark, J. S.; Robinson, I. K. Ultrafast Three-Dimensional Imaging of Lattice Dynamics in Individual Gold Nanocrystals. *Science* **2013**, *341*, 56–59.

(41) Assion, A.; Baumert, T.; Bergt, M.; Brixner, T.; Kiefer, B.; Seyfried, V.; Strehle, M.; Gerber, G. Control of chemical reactions by feedback-optimized phase-shaped femtosecond laser pulses. *Science* **1998**, *282*, 919–22.

(42) Vogt, G.; Krampert, G.; Niklaus, P.; Nuernberger, P.; Gerber, G. Optimal Control of Photoisomerization. *Physical Review Letters* **2005**, *94*, 068305.

(43) Herek, J. L.; Wohlleben, W.; Cogdell, R. J.; Zeidler, D.; Motzkus, M. Quantum control of energy flow in light harvesting. *Nature* **2002**, *417*, 533–535.

(44) Prokhorenko, V. I.; Nagy, A. M.; Waschuk, S. A.; Brown, L. S.; Birge, R. R.; Miller, R. J. D. Coherent control of retinal isomerization in bacteriorhodopsin. *Science* **2006**, *313*, 1257–61.

(45) Zhu, W.; Rabitz, H. A rapid monotonically convergent iteration algorithm for quantum optimal control over the expectation value of a positive definite operator. *The Journal of Chemical Physics* **1998**, *109*, 385–391.

(46) von den Hoff, P.; Thallmair, S.; Kowalewski, M.; Siemering, R.; de Vivie-Riedle, R. Optimal control theory âĂŞ closing the gap between theory and experiment. *Physical Chemistry Chemical Physics* **2012**, *14*, 14460.

(47) Goetz, R. E.; Karamatskou, A.; Santra, R.; Koch, C. P. Quantum optimal control of photoelectron spectra and angular distributions. *Physical Review A* **2016**, *93*, 013413.

(48) Keefer, D.; Mukamel, S. Selective Enhancement of Spectroscopic Features by Quantum Optimal Control. *Physical Review Letters* **2021**, *126*, 163202.

(49) Nass Kovacs, G. et al. Three-dimensional view of ultrafast dynamics in photoexcited bacteriorhodopsin. *Nature Communications* **2019**, *10*, 3177.

(50) Stankus, B. et al. Ultrafast X-ray scattering reveals vibrational coherence following Rydberg excitation. *Nature Chemistry* **2019**, *11*, 716–721.

(51) Cavaletto, S. M.; Keefer, D.; Rouxel, J. R.; Aleotti, F.; Segatta, F.; Garavelli, M.; Mukamel, S. Unveiling the spatial distribution of molecular coherences at conical intersections by covariance X-ray diffraction signals. *Proceedings of the National Academy of Sciences* **2021**, *118*, e2105046118.

(52) Weiner, A.; Leaird, D.; Patel, J.; Wullert, J. Programmable shaping of femtosecond optical pulses by use of 128-element liquid crystal phase modulator. *IEEE Journal of Quantum Electronics* **1992**, *28*, 908–920.

(53) Xiao, D.; Chang, M.-C.; Niu, Q. Berry phase effects on electronic properties. *Reviews of Modern Physics* **2010**, *82*, 1959–2007.

(54) Williamson, J. C.; Cao, J.; Ihee, H.; Frey, H.; Zewail, A. H. Clocking transient chemical changes by ultrafast electron diffraction. *Nature* **1997**, *386*, 159–162.

(55) Hastings, J. B.; Rudakov, F. M.; Dowell, D. H.; Schmerge, J. F.; Cardoza, J. D.; Castro, J. M.; Gierman, S. M.; Loos, H.; Weber, P. M. Ultrafast time-resolved electron diffraction with megavolt electron beams. *Applied Physics Letters* **2006**, *89*, 184109.

(56) Miller, R. J. D. Femtosecond Crystallography with Ultrabright Electrons and X-rays: Capturing Chemistry in Action. *Science* **2014**, *343*, 1108–1116.

(57) Yang, J. et al. Imaging CF 3 I conical intersection and photodissociation dynamics with ultrafast electron diffraction. *Science* **2018**, *361*, 64–67.

(58) Wolf, T. J. A. et al. The photochemical ring-opening of 1,3-cyclohexadiene imaged by ultrafast electron diffraction. *Nature Chemistry* **2019**, *11*, 504–509.

(59) Yang, J. et al. Simultaneous observation of nuclear and electronic dynamics by ultrafast electron diffraction. *Science* **2020**, *368*, 885–889.

(60) Yu, J. K.; Bannwarth, C.; Liang, R.; Hohenstein, E. G.; Martínez, T. J. Nonadiabatic Dynamics Simulation of the Wavelength-Dependent Photochemistry of Azobenzene Excited to the nπ^* and $\pi\pi^*$ Excited States. *Journal of the*

American Chemical Society **2020**, *142*, 20680–20690.

(61) Aquilante, F. et al. Molcas8: New capabilities for multiconfigurational quantum chemical calculations across the periodic table. *Journal of Computational Chemistry* **2016**, *37*, 506–541.

(62) Widmark, P.-O.; Malmqvist, P.-A.; Roos, B. O. Density matrix averaged atomic natural orbital (ANO) basis sets for correlated molecular wave functions. *Theoretica Chimica Acta* **1990**, *77*, 291–306.

(63) Berens, P. H.; Wilson, K. R. Molecular dynamics and spectra. I. Diatomic rotation and vibration. *The Journal of Chemical Physics* **1981**, *74*, 4872–4882.

(64) Thallmair, S.; Roos, M. K.; de Vivie-Riedle, R. Design of specially adapted reactive coordinates to economically compute potential and kinetic energy operators including geometry relaxation. *The Journal of Chemical Physics* **2016**, *144*, 234104.

(65) Reiter, S.; Keefer, D.; VivieâĂŘRiedle, R. *Quantum Chemistry and Dynamics of Excited States*; Wiley, 2020; pp 355–381.

(66) Tal-Ezer, H.; Kosloff, R. An accurate and efficient scheme for propagating the time dependent Schrödinger equation. *The Journal of Chemical Physics* **1984**, *81*, 3967–3971.

(67) Stephen Butterworth, On the Theory of Filter Amplifiers. *Experimental Wireless and the Wireless Engineer* **1930**, *7*, 536–541.

(68) Palao, J. P.; Kosloff, R. Optimal control theory for unitary transformations. *Physical Review A - Atomic, Molecular, and Optical Physics* **2003**, *68*, 13.

(69) Gollub, C.; Kowalewski, M.; de Vivie-Riedle, R. Monotonic Convergent Optimal Control Theory with Strict Limitations on the Spectrum of Optimized Laser Fields. *Physical Review Letters* **2008**, *101*, 073002.

Graphical TOC Entry